Balancing mass transfer and active sites to improve electrocatalytic oxygen reduction by B,N co-doped C nanoreactors

Xuefei Wang,[†§] Tianyi Liu,[ζ‡] Haitao Li,[†] Chao Han,[⊥] Panpan Su,[†] Na Ta,[†] San Ping Jiang,[#] Biao Kong,[ζ□] Jian Liu,[†,‡] and Zhenguo Huang[§*]*

[†] State Key Laboratory of Catalysis, Dalian Institute of Chemical Physics, Chinese Academy of Sciences, 457 Zhongshan Road, Dalian 116023, China

[§] School of Civil & Environmental Engineering, University of Technology Sydney, Sydney, NSW, 2007, Australia

[ζ] Department of Chemistry, Shanghai Key Lab of Molecular Catalysis and Innovative Materials, Collaborative Innovation Center of Chemistry for Energy Materials, Fudan University, Shanghai 200438, China

[‡] DICP-Surrey Joint Centre for Future Materials, Department of Chemical and Process Engineering, University of Surrey, Guildford, Surrey GU2 7XH, UK

[⊥] School of Materials Science and Engineering, Central South University, Changsha 410083, China

[#] Department of Minerals, Energy and Chemical Engineering, Fuels and Energy Technology Institute & WA School of Mines, Curtin University, Perth 6102, Australia

[] Yiwu Research Institute of Fudan University, Yiwu, Zhejiang 322000, China

KEYWORDS: oxygen reduction, nanoreactor, mass transfer, electrocatalysis

ABSTRACT: Mass transfer is critical in catalytic processes, more so when the reactions are facilitated by nanostructured catalysts. Strong efforts have been devoted to improving the efficacy and quantity of active sites, but often mass transfer has not been well studied. Herein, we demonstrate the importance of mass transfer in electrocatalytic oxygen reduction reaction (ORR) by tailoring the pore sizes. Using a confined-etching strategy, we fabricate boron- and nitrogen-doped carbon (B,N@C) electrocatalysts featuring abundant active sites but different porous structures. The ORR performance of these catalysts is found to correlate with the diffusion of the reactant. The optimized B,N@C with trimodal-porous structures feature enhanced O_2 diffusion and better activity per heteroatomic site toward the ORR process. This work demonstrates the significance of the nanoarchitecture-engineering of catalysts and also sheds light on how to optimize structure featuring abundant active sites and enhanced mass transfer.

INTRODUCTION

Carbon-based metal-free catalysts with stable structures, rich defects, and tunable electronic structures, have attracted much attention for various chemical reactions, including

thermocatalytic, electrocatalytic, and photocatalytic reactions. (1-2) In the past decades, numerous efforts have been devoted to optimizing the electronic structure of active centers at the nanoscale by heteroatom doping, especially with multiple heteroatoms. (3) Among these, boron and nitrogen co-doped carbon (B,N@C) has displayed interesting catalytic performance. (4-6) Most of the studies reported so far have focused on tuning chemical compositions and nanostructures to improve the efficacy and quantity of active sites.

An often less studied but significant factor affecting the catalytic process is mass transfer, which determines the efficiency of supply of reactants and removal of products to and from the active sites, and consequently the catalytic performance. For various gas-involving electrocatalysis, including hydrogen evolution reaction (HER), oxygen evolution reaction (OER), oxygen reduction reaction (ORR), electrochemical reduction of carbon dioxide (CO_2RR), and electrochemical reduction of nitrogen (N_2RR), the diffusion behavior of reactants and products plays a practical role in these heterogeneous catalysis process. So far, electrode fabrication and device configuration design have been the common approach to enhance mass transfer, (7-10) rather than tailoring the pore sizes and volumes of the nanocatalyst itself. (11-12)

Nanoreactors are effective platform materials with a wide range of structures where confined environments can modulate chemical reactions. (13-14) Trimodal porous nanoreactors with micropores (< 2 nm), mesopores (2−50 nm), and macropores (> 50 nm) are desirable to simultaneously achieve large numbers of active sites and improve mass diffusion. (15-18) Metal-organic frameworks (MOFs) are ideal precursors to obtain nanoreactors due to their customizable modular assembly and controllable morphologic and structural evolution. (1, 19-22) Key pore parameters including pore shapes, sizes, and volumes, can be regulated by controlling etching conditions. By varying the etching time, etching temperature, and etchant

concentration, mesopore sizes were confined within a range of 2-38 nm. (23-25) However, the range of pore sizes is not wide enough. Furthermore, pyrolyzing zinc-based MOFs (Zn-MOFs) has been used to obtain porous metal-free carbon materials with heteroatomic active sites. (26) However, most of these active sites are deeply hidden in the micropores of MOFs-derived nanocarbon and are unreachable for the catalytic reaction. (27) Selective etching of MOFs followed by pyrolysis proves effective in obtaining tunable nanostructures where active sites are exposed to reactants. (28-29) However, synthesizing a series of platform materials with different porous structures but similar active sites in efficacy and quantity is far less developed. Therefore, the relationship between mass transfer and catalytic activity is not well understood. B,N@C nanostructures have been derived by directly pyrolyzing B,N-containing MOF (e.g., boron imidazolate framework (BIF)-82 (30) and BIF-1S (31)) or MOFs mixed with B-containing substances (6, 32-40). Most of these MOF-derived B,N@C nanomaterials exhibit collapsed structures and narrow pore size distributions. (34-40) To obtain a great variety of pores with good controllability, this area is needed to study deeply including selecting the right precursors and the pyrolysis conditions.

Herein, we developed an effective method to fabricate porous three-dimensional (3D) B,N@C catalysts by sequentially etching and pyrolyzing a series of ZIF-8 precursors. It is known that most of the reported etching processes are too fast to precisely regulate the porosity of the MOF precursors. (28, 41) For example, tannic acid can transfer solid ZIF-8 and NH_2-MIL-125(Ti) into hollow MOFs in a very short period (< 30 min). (41) To adress this issue, ammonia borane (AB) which features mild hydrolysis was used to make the etching process controllable. Consequently, the structure of the B,N@C nanocages was effectively tailored. These 3D B,N@Cs feature similar catalytic active sites for ORR, in terms of chemical composition and quantity. But their

performance correlates with the porous structure, especially at the meso- and macroscale, which affects the mass transfer during the heterogeneous process. The performance of optimized B,N@C-24 catalyst is on par with commercial Pt/C, and the excellent catalysis is associated with the trimodal-porosity enabling the best combination of active site exposure and mass transfer.

RESULTS AND DISCUSSION

Synthesis of hierarchical porous B,N@C nanoreactors from modified ZIF-8 nanoparticles

The synthesis of B,N@C nanoreactors is illustrated in **Figure 1**. A double-solvent method was first used to immobilize ammonia borane (AB) as guest molecules in the ZIF-8 hosts on account of the immiscibility between water and cyclohexane. AB provides B and N as dopants and also acts as a mild etching agent by releasing protons during its slow hydrolysis, i.e., $NH_3BH_3 + 4H_2O \rightarrow NH_4^+ + B(OH)_4^- + 3H_2$. (29, 42) Therefore, compositional and structural modifications of ZIF-8 hosts were achieved at the same time, producing AB@ZIF-*x*h particles, where *x* represents the etching time. In the subsequent pyrolysis step, AB@ZIF-*x*h were transformed to corresponding B,N@C-*x*h nanocages with hierarchical porosities. (43)

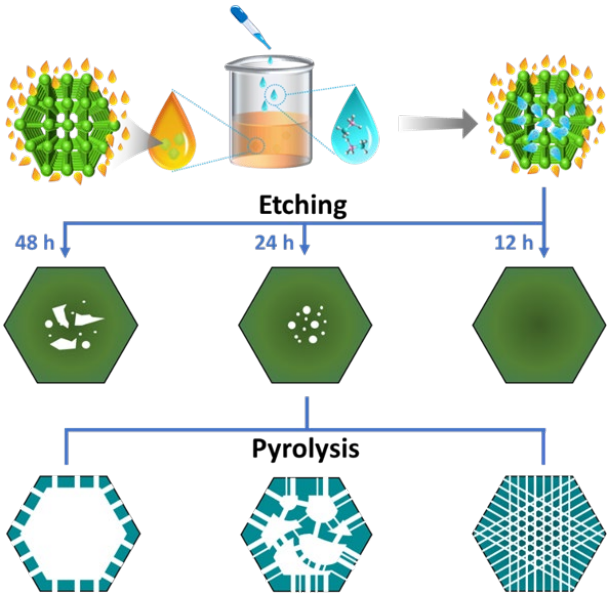

Figure 1. Schematics of the preparation of the B,N@C nanoreactors.

The X-ray diffraction (XRD) patterns of the resulting AB@ZIF-8 match the simulated powder XRD patterns based upon ZIF-8 single crystal (**Figure S1**). The scanning electron microscope (SEM) images show negligible changes in morphologies and sizes after etching (**Figure S2**). Transmission electron microscopy (TEM) images reveal the structural evolution of the AB@ZIF-8 nanoparticles through etching (**Figure 2a-c, S3**). AB@ZIF-2/6/12h nanoparticles retain the solid rhombic dodecahedron structure without obvious pores as the parent ZIF-8 (**Figure 2a and S3**). Extended etching gradually led to the formation of larger pores inside the host (**Figure 2b and c**). EDS mapping of AB@ZIF-24h in **Figure 2d** revealed that N and C were uniformly dispersed in the whole nanoparticle, while B and O were concentrated to the center of the particles, indicating that AB molecules were diffused inward through capillary action and hydrolyzed inside the host. These results prove that confined etching is effective in structurally modifying the MOF hosts.

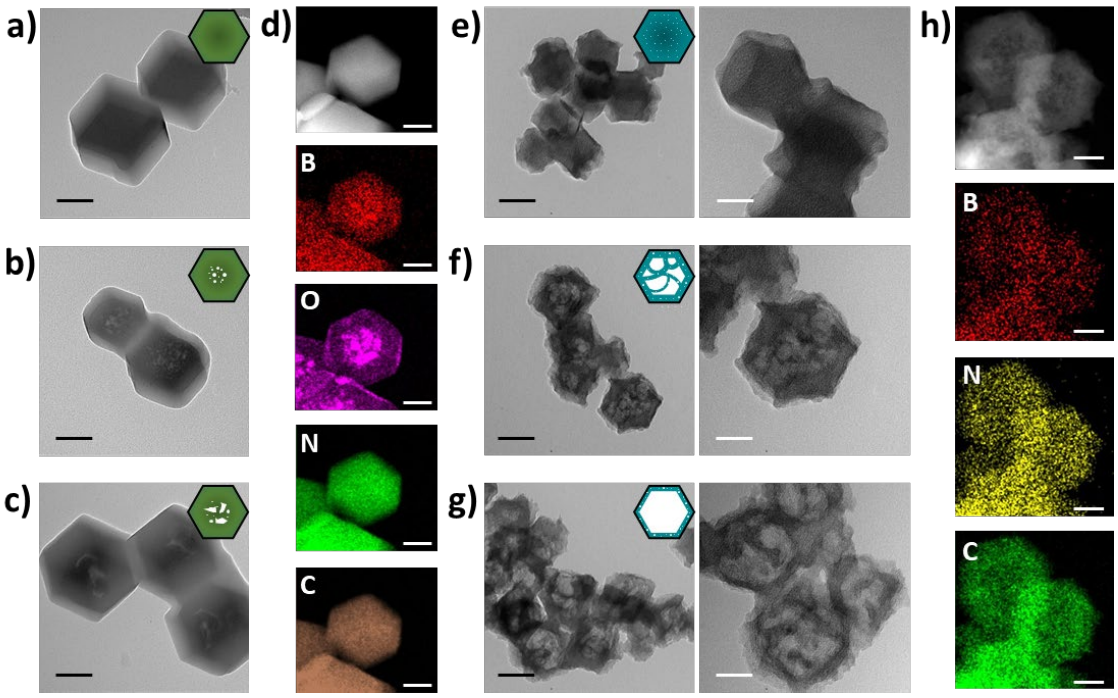

Figure 2. Controllable etching of ZIF-8 precursors and the derived hierarchical porous B,N@Cs. TEM images of (a) AB@ZIF-12h, (b) AB@ZIF-24h, (c) AB@ZIF-48h, (e) B,N@C-12h, (f) B,N@C-24h, and (g) B,N@C-48h. EDS mapping of (d) AB@ZIF-24h and (h) B,N@C-24h. Black and white scale bars are 100 and 50 nm, respectively.

Subsequently, B,N@C nanoreactors with different architectures were prepared by pyrolyzing the AB@ZIF-8 precursors at 1000 °C under N_2. As illustrated by SEM images in **Figure S4a**, B,N@C-12h retains polyhedral morphology similar to the AB@ZIF-12h precursor after pyrolysis. With the extension in etching, B,N@C became hollow and porous with rough surfaces

collapsed inward (**Figure S4b, c**). TEM images further verify the correlation between the nanoarchitecture of B,N@C (**Figure 2e-g**), and AB@ZIF-8 precursors (**Figure 2a-c**). Specifically, the greater degree the precursor was etched to, the larger cavities of the derived materials have. As a result, B,N@C-12h possesses small voids inside; B,N@C-24h transforms into nanocages with multiple compartments; B,N@C-48h becomes hollow cages. Elemental mapping images reveal that B and N heteroatoms are homogenously distributed together with C in all these structures. (**Figure 2h**), indicating the formation of uniform co-doping of C by B and N.

Structural relevance between AB@ZIF-8 precursors and the derived B,N@C

To further explore the structural dependency of B,N@C on AB@ZIF-8, their structures were evaluated using N_2 adsorption−desorption analysis (**Figure 3a,b**). The sorption isotherms of AB@ZIF-8 precursors (**Figure 3a**) display representative type I isotherms, indicating the dominance of micropores in these materials. The specific surface area decreased with longer etching, meaning that etching transformed some micropores into mesopores or macropores. (44) The pore size distribution profiles calculated based on non-local density functional theory (NLDFT) in **Figure S5** confirmed the decrease in micropore (< 2 nm) proportions and the increase in mesopore (2−50 nm) and macropore (> 50 nm) proportions during etching. N_2 adsorption−desorption isotherms were also collected to characterize the porosities of B,N@C nanocages (**Figure 3b**). Different from AB@ZIF-8, B,N@C exhibited a combination of type I and IV isotherms with clear hysteresis loops, indicating the existence of micro-, meso- and macropores. (18, 45) There are several possible mechanisms for the formation of porous B,N@C nanocages, which include the generation of gases, (46) the evaporation of Zn atoms, (47) and the generation of graphitic structure. (28) All the samples have undergone the same pyrolytic

conditions, so the differences in porous structures of B,N@C nanocages are mainly derived from the difference among the AB@ZIF-8 precursors.

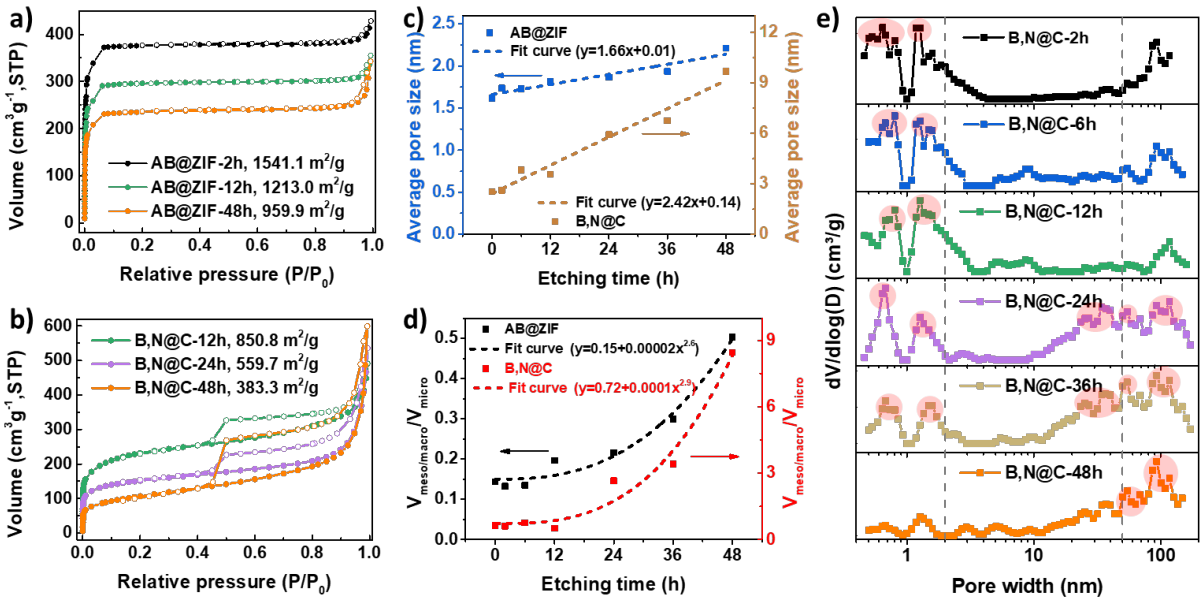

Figure 3. Structural characterization of AB@ZIF-8 nanoparticles and B,N@C nanocages. N_2 adsorption-desorption isotherms of a) AB@ZIF-8 and b) B,N@C, c) average pore size and d) pore volume ratios of meso/macro to micropore in AB@ZIF-8 and B,N@C, and e) pore size distributions of B,N@C.

To study the correlation of the porosity between AB@ZIF-8 nanoparticles and B,N@C nanocages, the relationship between their pore sizes and etching time was studied based on their

N_2 adsorption−desorption curves (**Figure 3a,b, and S6**). **Figure 3c** presents plots of average pore size versus etching time for AB@ZIF-8 and B,N@C, and the relationship between these two based upon curve fitting. For both AB@ZIF-8 and B,N@C, there is a linear correlation between the average pore size and etching time. The ratios of meso/macroporous to microporous volumes of AB@ZIF-8 precursors with etching time were also analyzed (**Figure 3d**). The difference in the first 6 hours is minimal, while the ratio increases faster after 12 hours, approximating to a power function relationship. This agrees well with the TEM images and confirms the essential role of AB in the host-guest chemistry-assisted etching to structurally modify the host so that B,N@C with tunable structures can be obtained. The ratio of meso/macroporous to microporous volumes of B,N@C nanocages shows a similar trend to that of AB@ZIF-8 and can be fitted to the power function with a similar power. These results bring out the feature of MOF-derived carbon, i.e., its architectures depending on the MOF precursors. However, most of the reported etching processes are too fast to precisely regulate the porosity of the parent MOFs. For example, tannic acid changed solid ZIF-8 and NH_2-MIL-125(Ti) into hollow MOFs in a very short time (< 30 min). (28, 41) In contrast, AB features mild hydrolysis which makes the etching process moderate and controllable. Consequently, the structure of the B,N@C nanocages can be effectively tailored.

The NLDFT pore size distribution analysis (**Figure 3e**) shows that B,N@C-2/6/12h samples mainly possess mainly micropores with sizes around 0.7 and 1.3 nm. B,N@C-24/36h samples present mesopores at about 25.3 and 37.1 nm, macropores at 93.1 and 117.2 nm, together with micropores at 0.7 and 1.3 nm, confirming them to be trimodal-porous. B,N@C-24h has a more balanced micro-, meso-, and macropores than that of B,N@C-36h. Macropores with the size of 54.4, 93.1, and 117.2 nm dominated in B,N@C-48h. These results indicate that B,N@C-

12/24/48h possess different nanoarchitectures, rendering them ideal material platforms to test the impact of porosity on mass transfer, and consequent ORR performance.

Characterization of B,N@C nanoreactors

B,N@C-12/24/48h were further investigated using XRD, Raman spectroscopy, and X-ray photoelectron spectroscopy (XPS) techniques. XRD patterns in **Figure 4a** show broad diffraction peaks at 25°, which could be indexed as the (002) crystal plane of amorphous carbon. (48) Raman spectra (**Figure 4b**) can be deconvoluted into four types of carbon configurations at 1,348 (D_1), 1,196 (D_2), 1,471 (D_3), and 1,577 (G) cm^{-1}. D_1, D_2, and D_3 bands are corresponding to the disordered carbon structure, amorphous carbon, and carbon atoms outside of a perfectly planar graphene network, respectively, while G band is attributed to the ordered graphite carbon. (49-50) The I_{D1}/I_G values for all the B,N@C nanoreactors are similar, within the range of 1.44 to 1.54, indicating their similar degree of graphitization and defects. Note that D_2 and D_3 bands contribute less to the ORR performance. (49) Chemical compositions and chemical states were analyzed with XPS. Survey scans show that all these catalysts contain B, C, N, and O (**Figure S7 and Table S1**). High-resolution XPS spectra of B 1s can be deconvolved into three peaks, which are assigned to B−C (190.6 eV), B−N (191.9 eV), and B−O (192.5 eV) (**Figure 4c and Table S2**). It is notable that, by prolonging the etching time, the proportion of B−O increased significantly from 0% in B,N@C-12h to 23% in B,N@C-48h, indicating the gradual accumulation of B−O during etching. This result matches well with our proposed etching mechanism that the mild hydrolysis of AB gradually releases protons, which then attack 2-MIM ligands in ZIF-8. For ORR, B−O bonds are reported to have a rather limited contribution to the performance, (51) where B−C and B−N benefit the ORR. (52-53) The N 1s XPS spectra are well fitted by five peaks, corresponding to N−B (397.9 eV), pyridinic N6 (398.5 eV), pyrrolic N5

(399.5 eV), graphitic N (400.8 eV), and N−O (402.4 eV). Pyridinic N6, pyrrolic N5 and graphitic N are also known to contribute to ORR. (54-55) The ratios of B (in B–N) to N species (in N–B) are similar in these catalysts (2.4 for B,N@C-12h, 2.5 for B,N@C-24h, and 2.5 for B,N@C-48h), but the total amounts of B and N in B,N@C-24h are slightly lower compared with the other two samples (**Table S2**). As shown in **Figure 4d** and **Table S2**, all these catalysts have similar chemical features of N and all these known active sites involving B and N are similar in ratio. Therefore, these three catalysts with similar heteroatomic $B_{2.5}$–N_1 motifs can serve as an ideal material platform to investigate the structure–performance relation of nanoreactors toward catalytic reactions.

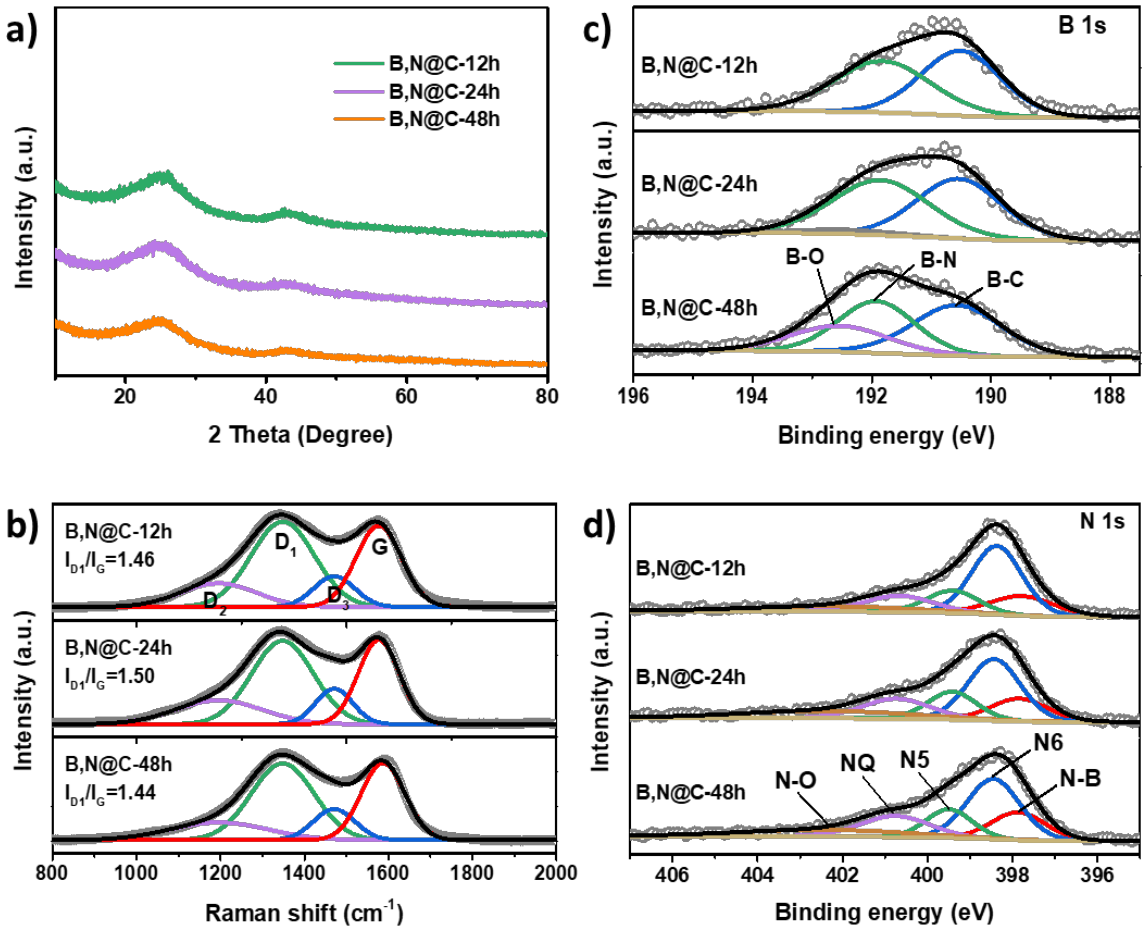

Figure 4. Characterization of the B,N@C nanoreactors. (a) PXRD patterns, (b) Raman spectra, (c) XPS spectra of B 1s, and (d) XPS spectra of N 1s.

Electrocatalytic ORR performance of B,N@C nanoreactors in relation to mass transfer

Electrochemical ORR was used as a model reaction to test the effect of porous structural engineering on the catalytic performance and to understand the importance of mass transfer during the reaction. The performance was assessed using a rotation ring disk electrode (RRDE) in a typical three-electrode system. The LSV disk curves collected at 1600 rpm in an O_2-saturated 0.01 M (pH = 12) and 0.1 M (pH = 13) KOH solution are shown in **Figure 5a** and **Figure 5b**, respectively. Generally, dilute electrolytes exhibit low viscosity, therefore having negligible effects on mass diffusion. As a result, the active site determines the electrocatalytic performance. As can be seen from **Figure 5a**, the difference in diffusion-limited current density (DLCD) among the three samples is negligible in the 0.01 M KOH solution. As expected, B,N@C-12h with the largest surface area shows the most positive half-wave potential ($E_{1/2}$) of 0.557 V vs. RHE (**Figure S8**), while B,N@C-48h with the lowest surface area shows the most negative $E_{1/2}$ of 0.524 V vs. RHE. These results confirm that the electrocatalytic performance is determined by the exposure of active sites in dilute electrolytes, which is typically related to surface areas. In contrast, the ORR performance of the three samples in 0.1 M KOH varies greatly (**Figure 5b and c**). It is known that when the electrolyte concentration increases, the viscosity of the electrolyte increases correspondingly (56) and the effect of mass transfer on catalytic performance becomes more significant. Therefore, the catalytic activity was determined by both the exposure of the active sites and the mass transfer efficiency. As shown in **Figure 5c**, B,N@C-24h with the most balanced trimodal-porous structure among the three catalysts (**Figure 5d**), achieved the largest diffusion-limited current density (DLCD) of −5.9 mA cm^{-2} at 0.2 V vs.

RHE. In addition, B,N@C-24h catalyst featured the most positive onset potential (E_{on}) of 0.979 V and $E_{1/2}$ of 0.861 V vs. RHE, as summarized in **Figure 5c**. The better ORR performance of B,N@C-24h than B,N@C-12h in 0.1 M KOH is mainly due to the enhancement of mass transfer in meso/macropores compared with micropores, demonstrating that mass transfer is vital for ORR in concentrated electrolyte solutions. Meanwhile, B,N@C-48h shows the low activity among these three catalysts, which indicates that mass transfer is not the only important factor in determining performance.

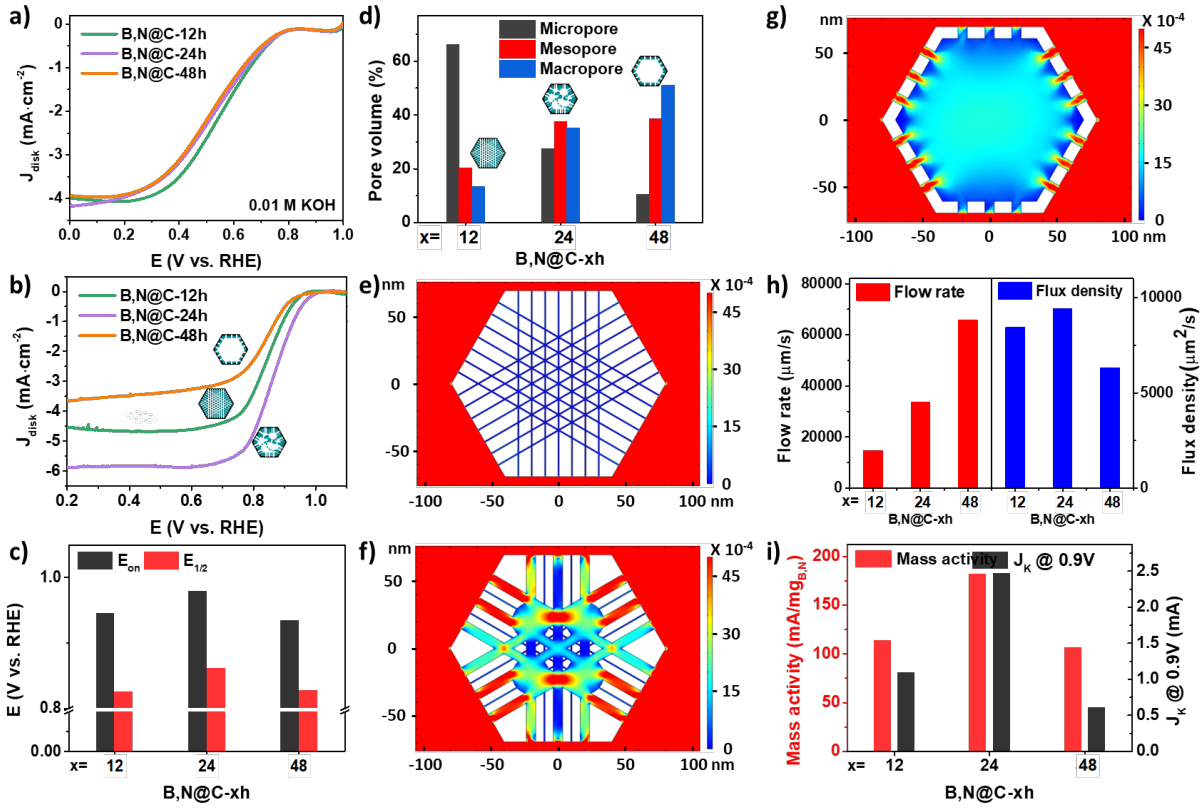

Figure 5. Electrocatalytic ORR performance of the B,N@C nanoreactors. (a) LSV curves in 0.01 M KOH; (b) LSV curves and (c) corresponding onset and half-wave potentials in 0.1 M KOH; (d) relative pore portions; velocity fields of nanoarchitecture models: e) B,N@C-12h, f) B,N@C-

24h, and g) B,N@C-48h; h) the simulated flow rate and flux density for B,N@C-12/24/48h, and i) mass-specific activities and kinetic current densities.

Finite element analysis (FEA) simulations were carried out to further understand the influence of mass transfer on electrocatalytic performance. According to the structural characterizations (**Figure 2 and 5d**), the main difference between the three samples is the pore sizes and volumes in the nanoreactor. Models were constructed to reflect the cavity size and porous channels. As shown in **Figure 5e-g**, the models exhibit micropore-dominated, balanced trimodal-porous, and macropore-dominated structures, corresponding to the experimentally synthesized B,N@C-12h, B,N@C-24h, and B,N@C-48h, respectively. The different color in **Figure 5e-g** is associated with the velocity of simulated flow fields. The flow velocity, which is significantly influenced by the geometric architectures of the materials, is an important index to evaluate mass diffusion. As expected, the flow rate in the macropore-dominated hollow cage is overall larger than that in the micropore-dominated and balanced trimodal-porous structures (**Figure 5h**), with only a few positions having rates similar to those of the trimodal-porous structures (**Figure 5f,g**). The electrochemical ORR process is mainly determined by the accessibility of active sites, which is affected not only by the mass transfer efficiency but also by the exposure of active sites. Therefore, the flux passing the entire internal surface was introduced (denoted as flux density hereafter), which takes into account both the active site exposure affected by the specific surface areas and the mass transfer determined by the porous structure. The flux density helps to investigate the process intensification by porous structural engineering of nanoreactors. The micro/meso/macropore-balanced model has a clear advantage over the other two models (**Figure 5h**). The flux density decreases significantly in the macropore-dominated hollow cage because of the limited surface area. Meanwhile, the flux density of the micropore-dominated sample is also

smaller than that of the trimodal-porous structure because of the limited mass transfer. On all these counts, trimodal-porous architecture is considered to be the desired nanoreactor to boost the process intensification.

As discussed above, B,N@C-24h with trimodal-porous structure delivered the largest E_{on}, $E_{1/2,}$ and DLCD among these three catalysts, and its performance is comparable to commercial Pt/C (**Figure S9**), which shows an E_{on} of 1.01 V, an $E_{1/2}$ of 0.867 V, and a DLCD of −5.6 mA cm^{-2} at 0.2 mV vs. RHE. Besides, the performance of B,N@C-24 nanoreactors is on par or even better than the reported metal-free carbon-based catalysts (**Table S3**). In contrast, micropore-dominated B,N@C-12h demonstrated lower E_{on}, $E_{1/2,}$ and DLCD than B,N@C-24h though it has the highest heteroatom content (**Table S1**). This suggests that certain active sites in the micropores have no contact with the reactants so the ORR rate is limited. (57) In addition, B,N@C-48h with a larger portion of macropores also shows decreased ORR activities compared with B,N@C-24h (**Figure 5b,c**), which is mainly due to reduced surface active sites. To further test the effect of porous structural engineering on process intensification toward ORR, heteroatomic mass activity and kinetic current density (J_K) were calculated. B,N@C-24h with trimodal-porous distributions delivers the highest mass-specific activity and J_k among the three catalysts (**Figure 5i**). In addition, B,N@C-24h possesses the lowest Tafel slope (**Figure S10**), further manifesting that the trimodal-porous nanoreactor exhibits the fastest kinetics toward ORR. All these results prove that a trimodal-porous nanoreactor is desired for improving both mass transfer and exposure of active sites. Based on RRDE measurement (**Figure S11a and Figure 5b**), the average electron transfer number (n) of B,N@C-24h was calculated to be about 3.83 (**Figure S11b**), indicating an efficient $4e^-$ pathway toward ORR, which is desirable for Zinc-air batteries. Similarly, electron transfer numbers were found for B,N@C-12h and B,N@C-48h.

CONCLUSION

We designed a series of hierarchical porous carbon nanoreactors doped with B and N via the efficient confined-etching and pyrolysis of ZIFs. The B,N@C nanocages have similar catalytic active sites in terms of intrinsic activity and quantity but have different pores in terms of size and volume. When tested for ORR, the B,N@C nanoreactor with abundant micro-, meso-, and macropores shows the highest catalytic activity. Experimental results and FEA calculations confirm that such trimodal-porous architecture enhances process intensification toward ORR because of enhanced mass transfer and effective active site exposure, in comparison with microporous and macroporous architectures. This work demonstrates the importance of mass transfer during heterogenous catalysis, which should be considered when designing novel catalysts. It also proves the efficacy of host-guest chemistry-assisted etching strategy, especially with mild etchants, for the synthesis of heteroatom-doped carbon nanoreactor systems.

ASSOCIATED CONTENT

Supporting Information

The Supporting Information is available free of charge at https://pubs.acs.org/doi/xxx.

Material, experimental and simulation details, additional characterization, and electrochemical performances (PDF)

AUTHOR INFORMATION

Corresponding Author

Jian Liu, jianliu@dicp.ac.cn, jian.liu@surrey.ac.uk

Zhenguo Huang, zhenguo.huang@uts.edu.au

Author Contributions

J.L., and Z.H. conceptualized the project. X.W. designed and performed most of the experiments and characterizations. T.L., and B.K. conducted the finite element analysis (FEA) simulation. N.T. performed the EDS mapping. P.S. helped with data processing and analysis. H.L. designed the Table of Contents (TOC) graphic. X.W. drafted the paper. C.H., P.S., S.J., Z.H. and J.L. revised the paper. All the authors discussed the results and commented on the manuscript.

Funding Sources

This work was supported by the National Natural Science Foundation of China (22279139, 21905271), Shanghai Science and Technology Committee (19DZ2270100), the National Key R&D Program of China (2021YFA1501900), the Australian Research Council's Future Fellowship (FT190100658). X. Wang also acknowledges the Chinese Scholarship Council (CSC) for financial support.

Notes

The authors declare no competing financial interest.

ACKNOWLEDGMENT

We acknowledge support from the National Natural Science Foundation of China (22279139, 21905271), Shanghai Science and Technology Committee (19DZ2270100), the National Key R&D Program of China (2021YFA1501900), the Australian Research Council's Future Fellowship (FT190100658). X. Wang also acknowledges the Chinese Scholarship Council (CSC) for financial support.

REFERENCES

(1) Wu, Z.; Li, Y.; Zhang, C.; Huang, X.; Peng, B.; Wang, G., Recent advances in metal-organic-framework-based catalysts for thermocatalytic selective oxidation of organic substances. *Chem Catalysis* **2022,** *2* (5), 1009-1045.

(2) Liu, X.; Verma, G.; Chen, Z.; Hu, B.; Huang, Q.; Yang, H.; Ma, S.; Wang, X., Metal-organic framework nanocrystal-derived hollow porous materials: Synthetic strategies and emerging applications. *The Innovation* **2022,** *3* (5), 100281.

(3) Zhang, S. L.; Guan, B. Y.; Lu, X. F.; Xi, S.; Du, Y.; Lou, X. W., Metal atom-doped Co_3O_4 hierarchical nanoplates for electrocatalytic oxygen evolution. *Adv. Mater.* **2020,** *32* (31), 2002235.

(4) Fang, Y.; Wang, X., Metal-free boron-containing heterogeneous catalysts. *Angew. Chem. Int. Ed.* **2017,** *56* (49), 15506-15518.

(5) Li, Z.; Chen, Y.; Ma, T.; Jiang, Y.; Chen, J.; Pan, H.; Sun, W., 2D metal-free nanomaterials beyond graphene and its analogues toward electrocatalysis applications. *Adv. Energy Mater.* **2021,** *11* (25), 2101202.

(6) Huang, P.; Li, H.; Huang, X.; Chen, D., Multiheteroatom-doped porous carbon catalyst for oxygen reduction reaction prepared using 3D network of ZIF-8/polymeric nanofiber as a facile-doping template. *ACS Appl. Mater. Interfaces* **2017,** *9* (25), 21083-21088.

(7) Chen, Q.-X.; Liu, Y.-H.; He, Z.; Wang, J.-L.; Liu, J.-W.; Jiang, H.-J.; Huang, W.-R.; Gao, G.-Y.; Hou, Z.-H.; Yu, S.-H., Microchemical engineering in a 3D ordered channel enhances electrocatalysis. *J. Am. Chem. Soc.* **2021,** *143* (32), 12600-12608.

(8) Zhang, Q.; Zhou, M.; Ren, G.; Li, Y.; Li, Y.; Du, X., Highly efficient electrosynthesis of hydrogen peroxide on a superhydrophobic three-phase interface by natural air diffusion. *Nat. Commun.* **2020,** *11* (1), 1731.

(9) Jung, E.; Shin, H.; Hooch Antink, W.; Sung, Y.-E.; Hyeon, T., Recent advances in electrochemical oxygen reduction to H_2O_2: Catalyst and cell design. *ACS Energy Lett.* **2020,** *5* (6), 1881-1892.

(10) Wang, P.; Hayashi, T.; Meng, Q. a.; Wang, Q.; Liu, H.; Hashimoto, K.; Jiang, L., Highly boosted oxygen reduction reaction activity by tuning the underwater wetting state of the superhydrophobic electrode. *Small* **2017,** *13* (4), 1601250.

(11) Jing, L.; Tian, Q.; Su, P.; Li, H.; Zheng, Y.; Tang, C.; Liu, J., Mesoporous Co–O–C nanosheets for electrochemical production of hydrogen peroxide in acidic medium. *J. Mater. Chem. A* **2022,** *10* (8), 4068-4075.

(12) Jing, L.; Tang, C.; Tian, Q.; Liu, T.; Ye, S.; Su, P.; Zheng, Y.; Liu, J., Mesoscale diffusion enhancement of carbon-bowl-shaped nanoreactor toward high-performance electrochemical H_2O_2 production. *ACS Appl. Mater. Interfaces* **2021,** *13* (33), 39763-39771.

(13) Zhu, W.; Chen, Z.; Pan, Y.; Dai, R.; Wu, Y.; Zhuang, Z.; Wang, D.; Peng, Q.; Chen, C.; Li, Y., Functionalization of hollow nanomaterials for catalytic applications: Nanoreactor construction. *Adv. Mater.* **2019,** *31* (38), 1800426.

(14) Wang, X.; Su, P.; Duyar, M. S.; Liu, J., Microenvironment and nanoreactor engineering of single-site metal catalysts for electrochemical CO_2 reduction. *Energy Fuels* **2021,** *35* (12), 9795-9808.

(15) Boyjoo, Y.; Shi, H.; Tian, Q.; Liu, S.; Liang, J.; Wu, Z.-S.; Jaroniec, M.; Liu, J., Engineering nanoreactors for metal–chalcogen batteries. *Energy Environ. Sci.* **2021,** *14* (2), 540-575.

(16) Sun, M.; Fu, Q.; Gao, L.; Zheng, Y.; Li, Y.; Chen, M.; Bao, X., Catalysis under shell: Improved CO oxidation reaction confined in Pt@h-BN core–shell nanoreactors. *Nano Research* **2017,** *10* (4), 1403-1412.

(17) Chen, H.; Shen, K.; Mao, Q.; Chen, J.; Li, Y., Nanoreactor of MOF-derived yolk–shell Co@C–N: Precisely controllable structure and enhanced catalytic activity. *ACS Catal.* **2018,** *8* (2), 1417-1426.

(18) Boyjoo, Y.; Shi, H.; Olsson, E.; Cai, Q.; Wu, Z.-S.; Liu, J.; Lu, G. Q., Molecular-level design of pyrrhotite electrocatalyst decorated hierarchical porous carbon spheres as nanoreactors for lithium–sulfur batteries. *Adv. Energy Mater.* **2020,** *10* (20), 2000651.

(19) He, S.; Chen, Y.; Zhang, Z.; Ni, B.; He, W.; Wang, X., Competitive coordination strategy for the synthesis of hierarchical-pore metal–organic framework nanostructures. *Chemical Science* **2016,** *7* (12), 7101-7105.

(20) Cheng, W.; Zhang, H.; Luan, D.; Lou, X. W., Exposing unsaturated Cu_1-O_2 sites in nanoscale Cu-MOF for efficient electrocatalytic hydrogen evolution. *Science Advances* **2021,** *7* (18), eabg2580.

(21) Dang, Q.; Li, Y.; Zhang, W.; Kaneti, Y. V.; Hu, M.; Yamauchi, Y., Spatial-controlled etching of coordination polymers. *Chin. Chem. Lett.* **2021,** *32* (2), 635-641.

(22) Lu, X. F.; Xia, B. Y.; Zang, S.-Q.; Lou, X. W., Metal–organic frameworks based electrocatalysts for the oxygen reduction reaction. *Angew. Chem. Int. Ed.* **2020,** *59* (12), 4634-4650.

(23) Kim, Y.; Yang, T.; Yun, G.; Ghasemian, M. B.; Koo, J.; Lee, E.; Cho, S. J.; Kim, K., Hydrolytic transformation of microporous metal–organic frameworks to hierarchical micro- and mesoporous MOFs. *Angew. Chem. Int. Ed.* **2015,** *54* (45), 13273-13278.

(24) Albolkany, M. K.; Liu, C.; Wang, Y.; Chen, C.-H.; Zhu, C.; Chen, X.; Liu, B., Molecular surgery at microporous MOF for mesopore generation and renovation. *Angew. Chem. Int. Ed.* **2021,** *60* (26), 14601-14608.

(25) Koo, J.; Hwang, I.-C.; Yu, X.; Saha, S.; Kim, Y.; Kim, K., Hollowing out mofs: Hierarchical micro- and mesoporous MOFs with tailorable porosity via selective acid etching. *Chemical Science* **2017,** *8* (10), 6799-6803.

(26) Song, X.; Jiang, Y.; Cheng, F.; Earnshaw, J.; Na, J.; Li, X.; Yamauchi, Y., Hollow carbon-based nanoarchitectures based on ZIF: Inward/outward contraction mechanism and beyond. *Small* **2020,** *17* (2), 2004142.

(27) Su, H.; Zhou, S.; Zhang, X.; Sun, H.; Zhang, H.; Xiao, Y.; Yu, K.; Dong, Z.; Dai, X.; Huang, X., Metal–organic frameworks-derived core–shell Fe_3O_4/Fe_3N@graphite carbon nanocomposites as excellent non-precious metal electrocatalyst for oxygen reduction. *Dalton Trans.* **2018,** *47* (46), 16567-16577.

(28) Zhang, W.; Jiang, X.; Zhao, Y.; Carné-Sánchez, A.; Malgras, V.; Kim, J.; Kim, J. H.; Wang, S.; Liu, J.; Jiang, J.-S.; Yamauchi, Y.; Hu, M., Hollow carbon nanobubbles: Monocrystalline MOF nanobubbles and their pyrolysis. *Chemical Science* **2017,** *8* (5), 3538-3546.

(29) Wang, X.; Han, C.; Li, H.; Su, P.; Ta, N.; Ma, Y.; Huang, Z.; Liu, J., Fabrication of monodispersed B, N co-doped hierarchical porous carbon nanocages through confined etching to boost electrocatalytic oxygen reduction. *Nano Research* **2023,** *16* (1), 290-298.

(30) Liu, M.-R.; Hong, Q.-L.; Li, Q.-H.; Du, Y.; Zhang, H.-X.; Chen, S.; Zhou, T.; Zhang, J., Cobalt boron imidazolate framework derived cobalt nanoparticles encapsulated in B/N codoped nanocarbon as efficient bifunctional electrocatalysts for overall water splitting. *Adv. Funct. Mater.* **2018,** *28* (26), 1801136.

(31) Qian, Y.; Hu, Z.; Ge, X.; Yang, S.; Peng, Y.; Kang, Z.; Liu, Z.; Lee, J. Y.; Zhao, D., A metal-free ORR/OER bifunctional electrocatalyst derived from metal-organic frameworks for rechargeable Zn-air batteries. *Carbon* **2017,** *111*, 641-650.

(32) Chen, X.; Xie, Y.; Shao, Y.; Shen, K.; Li, Y., Facile synthesis of boron and nitrogen dual-doped hollow mesoporous carbons for efficient reduction of 4-nitrophenol. *ACS Appl. Mater. Interfaces* **2021,** *13* (36), 42598-42604.

(33) Van Nguyen, C.; Lee, S.; Chung, Y. G.; Chiang, W.-H.; Wu, K. C. W., Synergistic effect of metal-organic framework-derived boron and nitrogen heteroatom-doped three-dimensional porous carbons for precious-metal-free catalytic reduction of nitroarenes. *Appl. Catal., B* **2019,** *257*, 117888.

(34) Li, Y.; Xu, H.; Huang, H.; Gao, L.; Zhao, Y.; Ma, T., Synthesis of Co–B in porous carbon using a metal–organic framework (MOF) precursor: A highly efficient catalyst for the oxygen evolution reaction. *Electrochem. Commun.* **2018,** *86*, 140-144.

(35) Tabassum, H.; Mahmood, A.; Wang, Q.; Xia, W.; Liang, Z.; Qiu, B.; zhao, R.; Zou, R., Hierarchical cobalt hydroxide and B/N co-doped graphene nanohybrids derived from metal-organic frameworks for high energy density asymmetric supercapacitors. *Sci. Rep.* **2017,** *7* (1), 43084.

(36) Tabassum, H.; Guo, W.; Meng, W.; Mahmood, A.; Zhao, R.; Wang, Q.; Zou, R., Metal–organic frameworks derived cobalt phosphide architecture encapsulated into B/N co-doped graphene nanotubes for all pH value electrochemical hydrogen evolution. *Adv. Energy Mater.* **2017,** *7* (9), 1601671.

(37) Zhang, H.; Ma, Z.; Duan, J.; Liu, H.; Liu, G.; Wang, T.; Chang, K.; Li, M.; Shi, L.; Meng, X.; Wu, K.; Ye, J., Active sites implanted carbon cages in core–shell architecture: Highly active and durable electrocatalyst for hydrogen evolution reaction. *ACS Nano* **2016,** *10* (1), 684-694.

(38) Wei, X.; Li, N.; Zhang, X., Co/CoO/C@B three-phase composite derived from ZIF67 modified with $NaBH_4$ solution as the electrocatalyst for efficient oxygen evolution. *Electrochim. Acta* **2018,** *264*, 36-45.

(39) Ahsan, M. A.; He, T.; Eid, K.; Abdullah, A. M.; Sanad, M. F.; Aldalbahi, A.; Alvarado-Tenorio, B.; Du, A.; Puente Santiago, A. R.; Noveron, J. C., Controlling the interfacial charge polarization of MOF-derived 0D–2D vdW architectures as a unique strategy for bifunctional oxygen electrocatalysis. *ACS Appl. Mater. Interfaces* **2022,** *14* (3), 3919-3929.

(40) Wan, Y.; Zhang, W.; Han, X.; Zhou, L.; Zhen, H.; Wu, C.; Yu, Q.; Xiu, G., B,N-decorated carbocatalyst based on Fe-MOF/BN as an efficient peroxymonosulfate activator for bisphenol a degradation. *J. Hazard. Mater.* **2022,** *430*, 127832.

(41) Sun, L.; Yuan, Y.; Wang, F.; Zhao, Y.; Zhan, W.; Han, X., Selective wet-chemical etching to create TiO_2@MOF frame heterostructure for efficient photocatalytic hydrogen evolution. *Nano Energy* **2020,** *74*, 104909.

(42) Brockman, A.; Zheng, Y.; Gore, J., A study of catalytic hydrolysis of concentrated ammonia borane solutions. *Int. J. Hydrogen Energy* **2010,** *35* (14), 7350-7356.

(43) Chang, F.; Su, P.; Guharoy, U.; Ye, R.; Ma, Y.; Zheng, H.; Jia, Y.; Liu, J., Edge-enriched N, S co-doped hierarchical porous carbon for oxygen reduction reaction. *Chin. Chem. Lett.* **2022**.

(44) Zhao, X.; Pachfule, P.; Li, S.; Simke, J. R. J.; Schmidt, J.; Thomas, A., Bifunctional electrocatalysts for overall water splitting from an iron/nickel-based bimetallic metal–organic framework/dicyandiamide composite. *Angew. Chem. Int. Ed.* **2018,** *57* (29), 8921-8926.

(45) Ma, X.; Du, J.; Sun, H.; Ye, F.; Wang, X.; Xu, P.; Hu, C.; Zhang, L.; Liu, D., Boron, nitrogen co-doped carbon with abundant mesopores for efficient CO_2 electroreduction. *Appl. Catal., B* **2021,** *298*, 120543.

(46) Yang, M.; Shu, X.; Zhang, J., A defect-rich N, P co-doped carbon foam as efficient electrocatalyst toward oxygen reduction reaction. *ChemCatChem* **2020,** *12* (16), 4105-4111.

(47) Song, X.; Zhang, H.; Yang, Y.; Zhang, B.; Zuo, M.; Cao, X.; Sun, J.; Lin, C.; Li, X.; Jiang, Z., Bifunctional nitrogen and cobalt codoped hollow carbon for electrochemical syngas production. *Advanced Science* **2018,** *5* (7), 1800177.

(48) Tang, J.; Salunkhe, R. R.; Liu, J.; Torad, N. L.; Imura, M.; Furukawa, S.; Yamauchi, Y., Thermal conversion of core–shell metal–organic frameworks: A new method for selectively functionalized nanoporous hybrid carbon. *J. Am. Chem. Soc.* **2015,** *137* (4), 1572-1580.

(49) Wang, K.; Chai, H.; Cao, Y., Using anion-exchange to induce the formation of edge defects in CoNx to enhance ORR activity. *ChemCatChem* **2022,** *14* (13), e202200146.

(50) Lai, Q.; Zheng, J.; Tang, Z.; Bi, D.; Zhao, J.; Liang, Y., Optimal configuration of N-doped carbon defects in 2D turbostratic carbon nanomesh for advanced oxygen reduction electrocatalysis. *Angew. Chem. Int. Ed.* **2020,** *59* (29), 11999-12006.

(51) Li, X.; Fan, L.; Xu, B.; Shang, Y.; Li, M.; Zhang, L.; Liu, S.; Kang, Z.; Liu, Z.; Lu, X.; Sun, D., Single-atom-like B-N_3 sites in ordered macroporous carbon for efficient oxygen reduction reaction. *ACS Appl. Mater. Interfaces* **2021,** *13* (45), 53892-53903.

(52) Wei, P.; Li, X.; He, Z.; Sun, X.; Liang, Q.; Wang, Z.; Fang, C.; Li, Q.; Yang, H.; Han, J.; Huang, Y., Porous N, B co-doped carbon nanotubes as efficient metal-free electrocatalysts for ORR and Zn-air batteries. *Chem. Eng. J.* **2021,** *422*, 130134.

(53) Zhang, M.; Tao, H.; Liu, Y.; Yan, C.; Hong, S.; Masa, J.; Robertson, A. W.; Liu, S.; Qiu, J.; Sun, Z., Ultrasound-assisted nitrogen and boron codoping of graphene oxide for efficient oxygen reduction reaction. *ACS Sustainable Chem. Eng.* **2019,** *7* (3), 3434-3442.

(54) Miao, H.; Li, S.; Wang, Z.; Sun, S.; Kuang, M.; Liu, Z.; Yuan, J., Enhancing the pyridinic N content of nitrogen-doped graphene and improving its catalytic activity for oxygen reduction reaction. *Int. J. Hydrogen Energy* **2017,** *42* (47), 28298-28308.

(55) Wu, J.; Ma, L.; Yadav, R. M.; Yang, Y.; Zhang, X.; Vajtai, R.; Lou, J.; Ajayan, P. M., Nitrogen-doped graphene with pyridinic dominance as a highly active and stable electrocatalyst for oxygen reduction. *ACS Appl. Mater. Interfaces* **2015,** *7* (27), 14763-14769.

(56) Goldsack, D. E.; Franchetto, A. A., The viscosity of concentrated electrolyte solutions—III. A mixture law. *Electrochim. Acta* **1977,** *22* (11), 1287-1294.

(57) Cao, Z.; Su, P.; Wang, X.; Liu, X.; Ma, Y.; Li, C.; Ping Jiang, S.; Liu, J., The structure–activity correlation of single-site Ni catalysts dispersed onto porous carbon spheres toward electrochemical CO_2 reduction. *Fuel* **2022,** *321*, 124043.

BRIEFS

Trimodal-porous B,N co-doped C nanoreactor is effective in enhancing process intensification during ORR by balancing mass transfer and exposure to active sites.

SYNOPSIS